JACS
JOURNAL OF THE AMERICAN CHEMICAL SOCIETY

Article

pubs.acs.org/JACS

Reaction Network of Layer-to-Tunnel Transition of MnO_2

Ye-Fei Li,* Sheng-Cai Zhu, and Zhi-Pan Liu*

Collaborative Innovation Center of Chemistry for Energy Material, Key Laboratory of Computational Physical Science (Ministry of Education), Shanghai Key Laboratory of Molecular Catalysis and Innovative Materials, Department of Chemistry, Fudan University, Shanghai 200433, China

Supporting Information

ABSTRACT: As a model system of 2-D oxide material, layered δ-MnO_2 has important applications in Li ion battery systems. δ-MnO_2 is also widely utilized as a precursor to synthesize other stable structure variants in the MnO_2 family, such as α-, β-, R-, and γ-phases, which are 3-D interlinked structures with different tunnels. By utilizing the stochastic surface walking (SSW) pathway sampling method, we here for the first time resolve the atomistic mechanism and the kinetics of the layer-to-tunnel transition of MnO_2, that is, from δ-MnO_2 to the α-, β-, and R-phases. The SSW sampling determines the lowest-energy pathway from thousands of likely pathways that connects different phases. The reaction barriers of layer-to-tunnel phase transitions are found to be low, being 0.2−0.3 eV per formula unit, which suggests a complex competing reaction network toward different tunnel phases. All the transitions initiate via a common shearing and buckling movement of the MnO_2 layer that leads to the breaking of the Mn−O framework and the formation of Mn^{3+} at the transition state. Important hints are thus gleaned from these lowest-energy pathways: (i) the large pore size product is unfavorable for the entropic reason; (ii) cations are effective dopants to control the kinetics and selectivity in layer-to-tunnel transitions, which in general lowers the phase transition barrier and facilitates the creation of larger tunnel size; (iii) the phase transition not only changes the electronic structure but also induces the macroscopic morphology changes due to the interfacial strain.

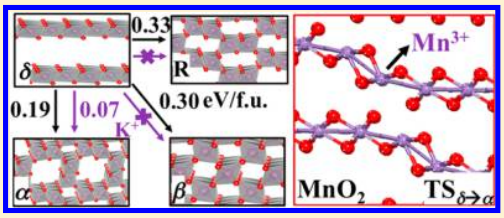

1. INTRODUCTION

MnO_2 is an important type of functional material in many applications, such as molecular sieves,[1] catalysts,[2,3] supercapacitors,[4,5] and Li/MnO_2 batteries.[6] One major feature of MnO_2 is its outstanding structural flexibility: many structural forms that differ in the crystallographic structure are stable at ambient conditions, including α-, β-, γ-, δ-, and R (Ramsdellite)-types, as shown in Figure 1.[7] The large tunnel structures are candidates of molecular sieve material,[1] while the layered structures are excellent cathode materials for ion storage in Li ion batteries due to the large interlayer spacing. Because the microscopic structure can influence markedly their physicochemical properties and thus the application, the controlled synthesis of MnO_2 polymorphs has long been a focus in material research. Our current knowledge of the pathway and the kinetics of these important solid-phase transformation processes is, however, surprisingly poor, which hinders the rational design of MnO_2 materials with desired properties.

Among the phases, δ-MnO_2 (hexagonal phase, $R\bar{3}M$) is quite special, with layered packing constituted by edge-sharing MnO_6 octahedra, and it can readily convert to other tunnel structures under synthetic conditions. α-MnO_2 (tetragonal, $I4/M$), β-MnO_2 (tetragonal phase, $P42/MNM$), R-MnO_2 (orthorhombic, $PNMA$), and γ-MnO_2 are distinguished by their different tunnel structures, namely, $[2 \times 2]$ for α-MnO_2, $[1 \times 1]$ for β-MnO_2, $[2 \times 1]$ for R-MnO_2, and both $[1 \times 1]$ and $[2 \times 1]$ for γ-MnO_2.[8] Not only edge-sharing but also corner-sharing MnO_6 octahedra are present in these tunneled MnO_2 structures. To date, great efforts have been devoted to trace the structural transformations in the conventional hydrothermal route to synthesize MnO_2 polymorphs by exploiting the redox reactions of MnO_4^-/Mn^{2+} in solutions.[9−11] Experiments by Wang and Li show that δ-MnO_2 acts as a common precursor to form other MnO_2 polymorphs such as α-, β-, γ-, and δ-MnO_2.[12] Zhou et al. also identified the formation of δ-MnO_2 from $Mn(NO_3)_2$ aqueous solution as early as 6 h under hydrothermal conditions, which further transforms into β-MnO_2 after 12 h.[13] It is now agreed that δ-MnO_2 is the kinetics' favored product that always forms first, and the other tunneled structures might be thermodynamically more favorable to form later via δ-MnO_2.[14] Therefore, the pathway and the kinetics of the phase transition from δ-MnO_2 to various MnO_2 polymorphs are not only scientifically interesting but also practically important, which dictate largely the morphology and the properties of MnO_2 material.

However, to date, few successes have been achieved to clarify the mechanism of the layer-to-tunnel transition since both high spatial and high temporal resolution are required. With time-resolved in situ synchrotron X-ray diffraction (XRD),[2,15] Shen et al.[15] identified R-MnO_2 as the intermediate phase in the δ to β transition under 1 M HNO_3 and 180 °C hydrothermal conditions, but they found no intermediate phase for δ-MnO_2 to a $[2 \times 4]$ tunnel MnO_2 under 1 M NaOH and 180 °C hydrothermal conditions. It implies that the transition may be a

Received: February 17, 2016
Published: April 7, 2016

DOI: 10.1021/jacs.6b01768
J. Am. Chem. Soc. 2016, 138, 5371−5379

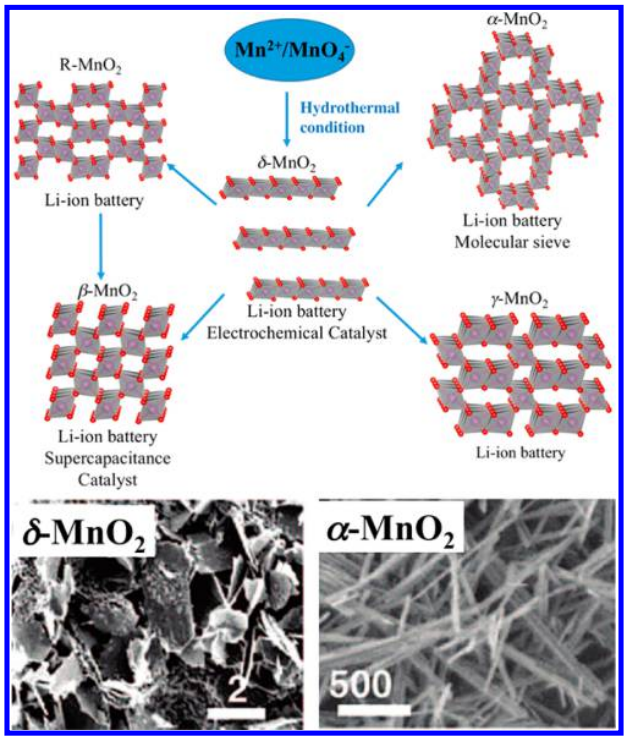

Figure 1. Top panel: atomic structures, synthesis conditions, and their applications for δ-MnO_2, α-MnO_2, β-MnO_2, γ-MnO_2, and R-MnO_2. Bottom panel: typical morphology for δ- and α-MnO_2 from scanning electron microscopy. Reprinted from ref 14. Copyright 2008 American Chemical Society.

multiple-step reaction and that the mechanism could be quite sensitive to the experimental conditions.

In this work, we report the first atomic mechanism of phase transition from δ-MnO_2 to other tunnel structures, α-, β-, and R-MnO_2. We utilized the newly developed global optimization method, stochastic surface walking (SSW) method, to sample the crystal phase space, exhaustively and unbiasedly, under both first-principles and empirical force-field frameworks. We identified the common structural and energetics features in the layer-to-tunnel phase transitions, rationalizing why δ-MnO_2 can act as the common precursor to form other tunnel structures. Importantly, the origin for the competing kinetics leading to different tunnel structures is discovered, which is further correlated to the movement pattern of critical Mn and O atoms.

2. THEORETICAL METHODS

2.1. Reaction Pathway Sampling Based on the SSW Method.

The SSW pathway sampling method was utilized to explore the structure transformation pathways of MnO_2 phases. The SSW pathway sampling combines the global structure search engine, SSW method,[16−18] and the pathway connection tool, double-ended surface walking (DESW) method.[19,20] The SSW is for collecting the likely pathways, aiming to identify the correct reaction coordinate for the low-energy pathway, and the DESW is to locate exactly the transition state (TS) of the pathway. The SSW pathway sampling can treat both aperiodic (molecules, clusters) and periodic (surfaces, crystals) systems. The method has been utilized recently to predict automatically the low-energy pathways of molecular reactions, surface restructuring, and crystal phase transitions.[21,22] The methodology detail can be found in our previous papers[17] and also in the Supporting Information. Here we briefly introduce the procedure of the pathway sampling.

The SSW pathway sampling starts from a particular phase of MnO_2 (e.g., δ-MnO_2), defined as the initial state (IS), and explores the structures nearby. All structures distinct from the IS, defined as the final state (FS), will be recorded, which will finally generate a database of IS/FS pairs, each defining a reaction coordinate. To ensure that the low-energy pathways are being sampled properly, we need to collect a large number of IS/FS pairs for each IS structure, typically up to 10^3 pathways within the first-principles framework and up to 10^5 pathways within the empirical force-field framework. It should be mentioned that the Euclidian distance between IS and FS is an important quantity to screen out the low-energy pathways from the large number of IS/FS pairs since a good structure match between IS and FS is a general requirement for low-energy pathways. Our previous study of ZrO_2 showed that the lowest-energy pathway usually has the shortest Euclidian distance between IS/FS pairs.[21]

By focusing on all the short distance pairs (e.g., <6 Å) and a few selected long-distance IS/FS pairs (e.g., <7 Å), we then utilized the variable-cell DESW method[16−18] to locate the TS explicitly between different MnO_2 phases. The criterion of distance for the low-energy pathway selection is based on our previous work on ZrO_2 and TiO_2 systems,[21,23] which showed that the typical length of the lowest-energy pathway is around 0.2 Å per atom (i.e., 5 Å for a unit cell of 8MnO_2). The TS is confirmed by extrapolating the TS toward the IS and FS and the numerical vibrational frequency analysis. The lowest-energy pathways are thus determined according to the located TSs by sorting the calculated barrier, which is the energy difference between the TS and the IS. The animations of transition pathways are provided in Supporting Information.

Table 1. Geometry, Electronic Structure, and Relative Energetics (ΔE) for All MnO_2 Polymorphs (with 8 MnO_2 fu) during Phase Transitions

structure	Mn−O[a] (Å)	E_g (eV)	magnetic order[b]	local spin moments on Mn[c] (μ_B)	tunnel size	V (Å^3)	ΔE (eV/fu)
δ-MnO_2	1.94	2.5	FM	3.12	layer	292	0
TS1	2.34	1.1	FM	3.34	layer	289	0.17
MS1	1.95	2.2	FiM	3.03	2 × 6	311	−0.01
TS2	2.24	1.1	FiM	3.65	2 × 6	289	0.18
α-MnO_2	1.92	2.2	AFM	3.03	2 × 2	287	−0.08
TS3	2.65	1.0	FM	3.76	layer	271	0.28
MS2	1.94	1.6	FiM	2.93	3 × 1	253	−0.04
TS5	2.36	1.0	FiM	3.62	3 × 1	268	0.30
R-MnO_2	1.92	2.2	AFM	3.13	2 × 1	255	−0.08
TS4	2.51	0.3	FiM	3.74	3 × 1	250	0.28
β-MnO_2	1.92	0.5	AFM	2.98	1 × 1	235	−0.03

[a]Listed are the typical equilibrium Mn−O bond lengths at stable states and the breaking/forming Mn−O distances at TSs. [b]FM = ferromagnetic, AFM = antiferromagnetic, FiM = ferrimagnetic. [c]The maximum local spin moment of Mn in crystals.

DOI: 10.1021/jacs.6b01768
J. Am. Chem. Soc. 2016, 138, 5371−5379

2.2. Calculation Details for MnO_2 Systems. Both the classical force-field potential (modified Matsui−Akoagi, mMA) model[24] and density functional theory (DFT) calculations have been utilized for MnO_2 systems. While DFT calculations are utilized both for SSW pathway sampling and for computing energetics of all low-energy pathways, we also supplement the IS/FS database by using the mMA force-field potential calculations in SSW pathway sampling to collect more than 10^5 pathways. As also shown in the previous work, the mMA potential can yield correct crystal structures of α-MnO_2, β-MnO_2, γ-MnO_2, and δ-MnO_2 that are in good agreement with experimental data.[25,26]

All DFT calculations were carried out within the periodic plane wave framework as implemented in the Vienna ab initio simulation package (VASP).[27] The electron−ion interaction was represented by the projector-augmented wave[28] (PAW), and the kinetic energy cutoff of the plane wave was set as 500 eV. The geometry optimization including the TS location was based on the exchange-correlation functional GGA-PBE[29] with on-site Coulomb repulsion (PBE+U).[30] All energetics were further recomputed using the hybrid functional HSE06.[31] The effective U−J terms (U_{eff}) as determined by linear response theory[32] were set to 4.0 eV for Mn. The geometry convergence criterion was set as 0.01 eV/Å for the maximal component of force and 0.01 GPa for stress. For all MnO_2 systems, spin-polarization has been considered to identify the ground-state electronic configuration. We found that δ-MnO_2 is ferromagnetic, but β- and R-MnO_2 are antiferromagnetic (see Table 1). The most stable spin configuration of the phase is thus system-dependent. Nevertheless, the energy differences between the ferromagnetic and the antiferromagnetic solutions are generally small, below 0.04 eV per MnO_2 formula unit (fu), and their effect to the reaction barrier is below 0.03 eV/fu. The ground-state magnetic ordering of the materials identified under the DFT+U scheme and HSE06 scheme are listed in the Supporting Information. The k-point mesh utilized was up to (2 × 8 × 4) in the Monkhorst−Pack scheme, which was verified to be accurate enough for these bulk systems.

2.3. Computational Models. The bulk structure of all MnO_2 phases can be straightforwardly optimized from first principles. It should be emphasized that although the crystal structures of β- and R-MnO_2 are known in the experiment (also see Supporting Information Table S1), some MnO_2 phases, such as δ- and α-MnO_2 phases in pure MnO_2 composition, are in fact uncertain in the crystal structure due to the general presence of intercalated species, such as K^+, Na^+, or NH_4^+[12,33] inside the MnO_2. Considering that these intercalated species are mobile and not present in the skeleton, we here, for simplicity, first focus on the phase transition of pure MnO_2 using exhaustive SSW pathway sampling, and the effect of the intercalated species is then studied based on the lowest-energy pathway obtained from the pure MnO_2 phases. For γ-MnO_2, since its structure can be considered as a mix of β- and R-phases, its formation from δ-phase can be represented by the δ to β and δ to R transition. We therefore did not investigate the δ to γ transition independently.

In all SSW pathway samplings, we always use the medium-sized unit cell of Mn_8O_{16} to identify the low-energy pathways between phases, which were found to be enough to capture the lowest-energy pathways. The pathway sampling with larger unit cells has also been examined using the empirical force field, which yields the same low-energy pathway.

3. RESULTS AND DISCUSSIONS

3.1. Structures and Thermodynamics. As the starting point, we calculated the bulk structure of different MnO_2 phases. The crystal parameters of these crystals were compared with the experimental data if available (see Supporting Information Table S1). In general, we found that DFT calculations at the PBE+U level can produce good crystal structures, including the lattice parameters and the Mn−O bond distances in the MnO_6 octahedron. In particular, the optimized lattice edge is close to the experimental data, with the difference being less than 3.2%, a typical error in DFT PBE calculations. We also noticed that despite the large difference in crystal structure of these phases (see tunnel size in Table 1), their Mn−O bond lengths are, in fact, rather similar, being ∼1.92−1.94 Å. These indicate the similar electronic configuration of Mn (i.e., Mn^{4+}) and the similar octahedral coordination environment in different phases.

On the other hand, the PBE+U calculations tend to underestimate the band gap of MnO_2.[34] For this, we always utilized the hybrid DFT at the HSE06 level to compute the energetics and the band structure of MnO_2, which has been shown to describe more reasonably the electronic structures and energetics for β-MnO_2.[34] In Table 1, we show that the DFT total energy of δ-, α-, β-, and R-MnO_2 lies closely to the energy difference (ΔE) between them within 0.08 eV/fu. The band gap, by contrast, can be rather sensitive to the crystal structure. In particular, the band gap of β-MnO_2, the phase with the smallest tunnel size ([1 × 1]), is only 0.5 eV, which is more than 1.5 eV narrower than the other phases.

It should be mentioned that the small energy differences between phases (thermodynamics) are consistent with the fact that all of the MnO_2 can exist at ambient conditions. The relative portion of phases could be tuned in experiment by modifying synthetic conditions, such as by utilizing different precursors, adding template species, or changing the ratio of reactant.[35,36] For example, R- and β-MnO_2 can be synthesized from δ-MnO_2 under 1 M HNO_3 and 180 °C hydrothermal conditions, whereas α-MnO_2 is obtained at 120 °C hydrothermal conditions starting from low crystalline MnOOH.[14] Dong et al. controlled the ratio of Mn^{2+}/MnO_4^- and synthesized either β-MnO_2 (ratio = 7:3) or α-MnO_2 (ratio =5:5) at 160 °C hydrothermal conditions.[33] It is therefore of more interest to explore the kinetics of transition between these phases.

3.2. Electronic Structures and Conductivities. To further reveal the difference in the electronic structure between the layered phase and three tunneled phases, we plotted the spin-resolved density of states (DOS) of δ-, α-, β-, and R-phases. As shown in Figure 2, we found that δ-MnO_2 has a distinct electronic structure compared to other tunneled phases. First, δ-MnO_2 is predicted to be ferromagnetic (FM), while the other three tunneled phases (α, β, R) are antiferromagnetic (AFM). This could be caused by the different connectivity pattern linking MnO_6 octahedra between δ-MnO_2 and other phases. All MnO_6 octahedra are edge-sharing in δ-MnO_2 but corner-sharing in β-MnO_2, while R-MnO_2 consists of 50% edge-sharing and 50% corner-sharing octahedra. Importantly, the Mn−O−Mn in edge-sharing MnO_6 is 98°, which is significantly smaller than that (129°) in the corner-sharing MnO_6. This leads to superexchange antiferromagnetic coupling[37,38] between two corner-sharing MnO_6 much stronger than that in the edge-sharing MnO_6. As a result, δ-MnO_2 prefers the FM ground state, while the spins of two corner-sharing MnO_6 prefer to be antiparallel, leading to the AFM spin-ordering.

Second, the conduction band (CB) and the valence band (VB) of δ-MnO_2 are narrower compared to those of other phases. In particular, the CB of δ-MnO_2 splits into two spin components, and both of them are much narrower (bandwidth ∼1.3 and 2.8 eV) than their counterparts in the other phases (>4.2 eV). Since the CB width is closely related to the conductivity of the electron carriers, it is therefore expected that, on going from the layer to the tunnel structures, the

DOI: 10.1021/jacs.6b01768
J. Am. Chem. Soc. 2016, 138, 5371−5379

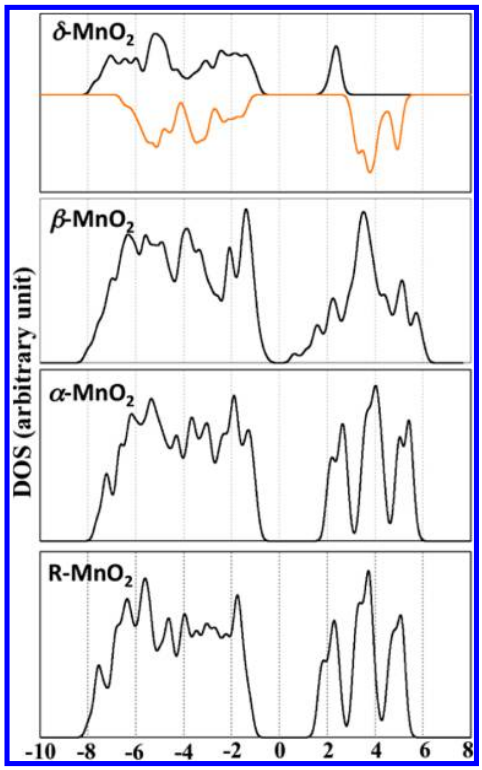

Figure 2. Spin-resolved density of states for four different MnO_2 phases. For FM δ-MnO_2, the DOS of both a majority and minority spins are displayed. Black lines are the majority spin, and red lines are the minority spin.

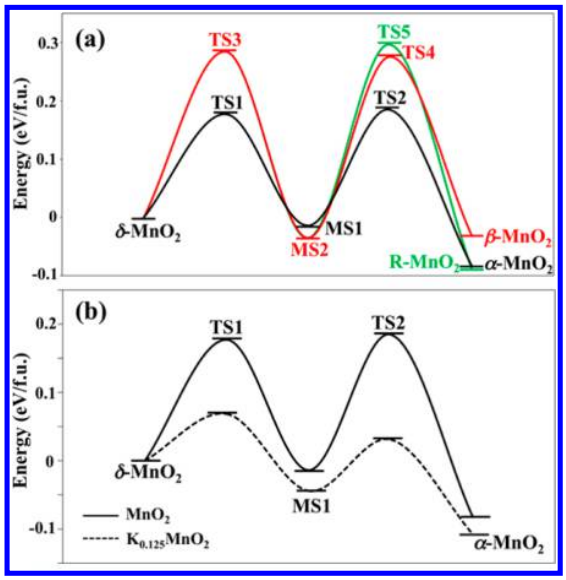

Figure 3. (a) Energetic profiles of pure MnO_2 transition from δ- to α-phase (black curve), β-phase (red curve), and R-phase (green curve). (b) Energetic profiles for $K_{0.125}MnO_2$ transition from δ- to α-phase, where K^+ cations are present initially in the interlayer spacing.

electric conductivity of material can be significantly improved, which is of great importance to battery performance (e.g., Li/MnO_2). Indeed, previous experiments have shown that when δ-MnO_2 transforms to tunneled structures such as [1 × 1], [2 × 2], [2 × 3], [2 × 4], etc., the electric resistivity can decrease by at least 2 orders of magnitude,[14,39] which suggests that δ-MnO_2 has conductivity much poorer than that of other tunneled phases. Several groups have measured the relative electric conductivity of various tunneled structures and found the order to be [3 × 3] ≪ [2 × 4] < [2 × 3] < [2 × 2] < [1 × 1].[14,39]

The larger CB width for the tunneled structures is also consistent with their shorter Mn−O bond length for corner-sharing MnO_6 octahedra. In δ-MnO_2, all Mn−O bonds are 1.94 Å, while in α-, β-, and R-phases, the Mn−O bonds of the corner-sharing MnO_6 octahedra shorten to 1.92 Å (the Mn−O bonds are still 1.94 Å in the edge-sharing MnO_6 octahedra). The increased covalent bonding between Mn cations and O anions leads to the larger 3d(Mn)−2p(O) orbital mixing and thus the larger bandwidth, the feature that is prominent in β-MnO_2.

3.3. Phase Transition Kinetics and Mechanisms. Using the SSW pathway sampling, we then investigated the mechanism and kinetics for the phase transition starting from δ-phase to the α-, β-, and R-phases. The energetic profiles corresponding to the lowest-energy pathway are shown in Figure 3, and the associated atomic movement patterns are drawn in Figure 4.

The variation of the electronic structure of MnO_2 during phase transition can be clearly seen from the local spin moment of Mn. For the four MnO_2 polymorphs, the local spin moment is ∼3 μ_B (see Table 1), consistent with the formal charge of Mn ($3d^5 4s^2$) being +4. For all the TSs in the phase transition, the local spin moments of Mn at the reaction center are significantly larger than ∼3 μ_B, indicating that these Mn ions are reduced during phase transition. This is obviously related to the Mn−O bond breaking during the phase transition. For instance, at TS2 for the δ to α transition, the spin moment of Mn at the reaction center increases to ∼3.7 μ_B (Mn^{3+}), while the spin moment of other Mn atoms remains at ∼3 μ_B (Mn^{4+}). This indicates that an electron transfers from adjacent O atoms to the Mn in the reaction.

More importantly, our calculations show that the phase transition barriers of the layer-to-tunnel transition are low, in general, around 0.2−0.3 eV/fu, which is consistent with the fact that all of these reactions can occur at ambient conditions. The atomic movement pattern during the transition is the key for understanding different kinetics for these phase transitions, which will be elaborated in the following sections.

3.3.1. δ to α Transition. The δ- to α-phase transition is not a direct reaction but mediated by an intermediate phase (monoclinic, $C2/M$), MS1 (see Figures 3 and 4). MS1 has a stability similar to that of the δ-phase. Being already a tunneled structure, it has both large [2 × 6] and small [1 × 1] tunnels. The first step from δ to MS1 and the second step from MS1 to α have similar reaction barriers, that is, 0.17 and 0.19 eV/fu.

Microscopically, the phase transition initiates via the translation and buckling of the δ-MnO_2 sheet (i.e., the (0001) basal plane). The shearing movement along the [$\bar{2}$021] direction that is 72° with respect to the sheet plane leads to the formation of Mn−O bonding between neighboring layers. This is shown clearly in the TS1, where the distortion of the Mn sublattice is localized in a small region, as highlighted by the red square domain in Figure 4. Four Mn−O bonds break within the red square domain (per 16 fu of MnO_2 layer), resulting in the formation of four 5-coordinated Mn (Mn_{5c}) and four 2-coordinated O (O_{2c}) at TS1. After TS1, the Mn_{5c} creates new bonds with O_{2c} at the neighboring MnO_2 sheet,

DOI: 10.1021/jacs.6b01768
J. Am. Chem. Soc. 2016, 138, 5371−5379

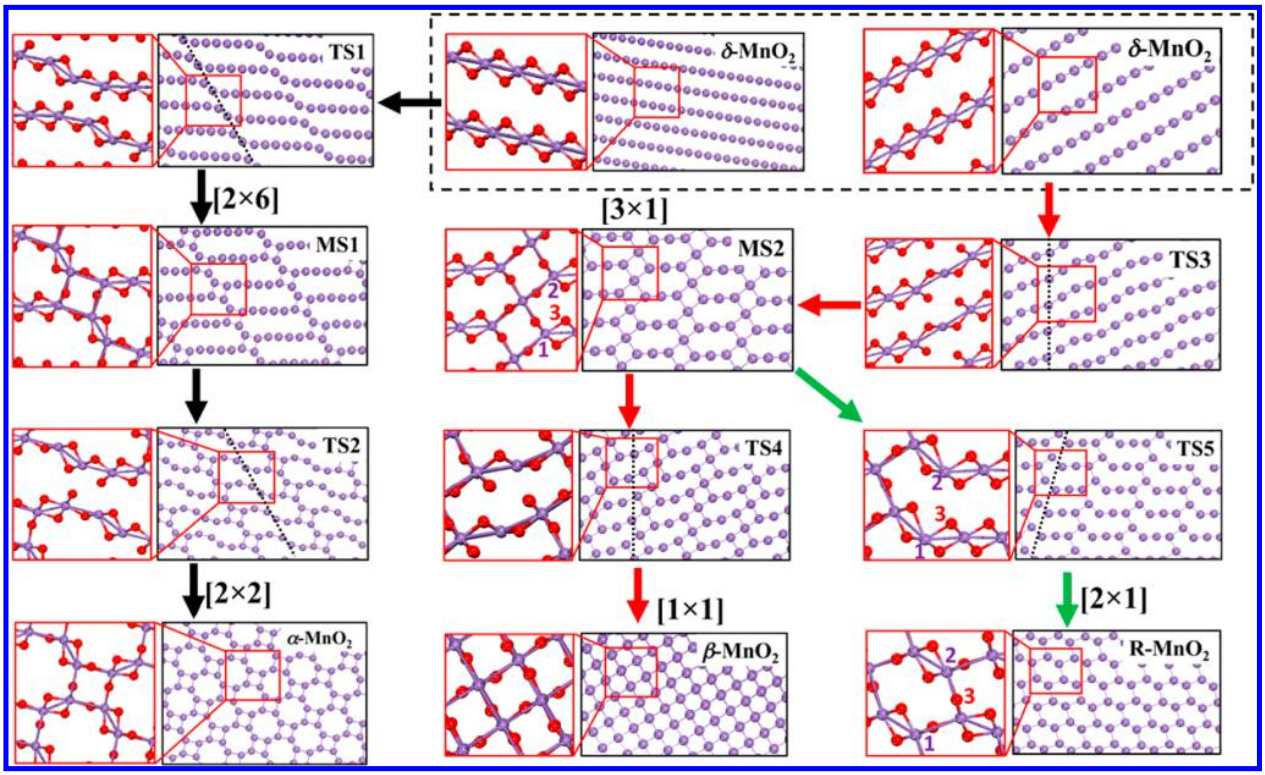

Figure 4. Snapshots of the key states (see Figure 3) in the δ- to α- (left), δ- to β- (middle), and δ- to R-phase (right) transitions. For the stable states, the largest sizes of tunnels are indicated. The purple ball and stick represent the Mn sublattice. In the right column of each picture, only the Mn sublattice is depicted to show clearly how Mn atoms move during phase transitions. The left column of each picture is the enlarged ball-and-stick representation for the red square box region of the right column picture. This local view highlights the large rearrangement of Mn−O frameworks in the phase transition. All pictures are viewed down at $[\bar{1}2\bar{1}0]_\delta$ direction. The dotted lines at TSs indicate the planes of shear displacement.

which forms the short sidewalls of [2 × 6] tunnels. Consequently, the undistorted Mn chains form the long sidewalls of [2 × 6] tunnels (see MS1, Figure 4).

In the step 2, the long sidewalls of the [2 × 6] tunnel experience a shear distortion similar to that in step 1. As a result, the [2 × 6] tunnel is separated into two [2 × 2] tunnels and one [1 × 1] tunnel, leading to the formation of the α-phase. After the δ to α transition, the basal plane $(0001)_\delta$ evolves into $(100)_\alpha$, that is, $(0001)_\delta$ parallel to $(100)_\alpha$, denoted as $(0001)_\delta//(100)_\alpha$, and the overall crystallographic orientation relation can be summarized as $(0001)_\delta//(100)_\alpha$ and $[\bar{1}2\bar{1}0]_\delta//[010]_\alpha$. By performing the strain analysis using the finite strain theory (see our previous work[21]), we found that the $(0001)_\delta//(100)_\alpha$ interface has very low strain and less than 1% lattice mismatch, which indicates that the two phases can form a stable heterophase junction.[40]

3.3.2. δ to β Transition. The lowest-energy pathway from the δ- to β-phase transition is different than that of the δ to α transition in the atom displacement pattern. The δ- to β-phase transition is also a two-step reaction involving an intermediate MS2 (monoclinic phase, $P2/M$) composed of [3 × 1] and [1 × 1] tunnels. The calculated barriers for the two steps are 0.28 and 0.30 eV/fu, which are systematically higher than those in the δ- to α-phase transition.

While the δ- to β-phase also requires the buckling of the MnO_2 basal plane, the major difference between the δ- to β- and the δ- to α-phase transition is the shearing direction. From δ to MS2, the MnO_2 basal planes shear along the $[0\bar{1}11]$ direction, which leads to the formation of interlinked [1 × 1] tunnels (see Figure 4, TS3). This is different from the $[\bar{2}021]$ direction shearing and resulted in separated [1 × 1] tunnels in the δ- to α-phase transition. Specifically, in the δ- to β-phase transition, the buckling of Mn chains will break four Mn−O bonds per 8 fu in the MnO_2 layer, resulting in the formation of Mn_{4c} and O_{2c} at TS3, as shown in the highlighted red square domain (Figure 4). The nascent Mn_{4c} then reconnects with two O_{2c} atoms in two neighboring MnO_2 layers to form MS2. The appearance of lower-coordinated Mn_{4c} in the δ- to β-phase transition explains the higher barrier of δ- to β-phase transition compared to that of δ- to α-phase transition. It should be mentioned that the δ to MS2 transition is also the first step in the δ to R transition that will be discussed below.

From MS2 to β-MnO_2, the long sidewalls of the [3 × 1] tunnel continue to shear along the same $[0\bar{1}11]_\delta$ direction, which finally transforms the [3 × 1] tunnel into three smaller [1 × 1] tunnels. Overall, δ to β transition obeys the crystallographic orientation relation of $(10\bar{1}1)_\delta//(100)_\beta$ and $[\bar{1}2\bar{1}0]_\delta//[010]_\beta$. The $(0001)_\delta$ basal plane transforms to $(110)_\beta$. According to the strain analysis, we noticed that $(0001)_\delta//(110)_\beta$ cannot form a stable interface between two phases due to the large lattice mismatch (20% strain). Instead, the $(10\bar{1}1)_\delta//(100)_\beta$ interface is energetically favorable with only 3.2% strain.

3.3.3. δ to R Transition. The lowest-energy pathway from δ- to R-phase transition shares a common intermediate with the δ to β transition. The δ- to R-phase transition consists of two steps, and the first step is exactly the same as the first step in the δ- to β-phase transition, that is, forming the MS2 intermediate.

DOI: 10.1021/jacs.6b01768
J. Am. Chem. Soc. 2016, 138, 5371−5379

Starting from MS2, the transition to R-MnO_2 has a barrier of 0.33 eV/fu, which is also close to that of the MS2- to β-phase transition.

The atom displacement pattern from MS2 to R-MnO_2 is therefore different from the transition to β-MnO_2. The $[1 \times 1]$ tunnels of MS2 reopen and merge with the $[3 \times 1]$ tunnels to form the distorted $[4 \times 1]$ tunnels (as shown in TS5 in Figure 4). Specifically, as shown by the labeled Mn and O atoms in the red square at TS5, the transition mainly involves the Mn(1)−O(3) bond break and the O(3)−Mn(2) bond formation. Overall, the δ to R transition occurs following the orientation relation of $(10\bar{1}1)_\delta//(100)_R$ and $[\bar{1}2\bar{1}0]_\delta//[010]_R$. The $(10\bar{1}1)_\delta//(100)_R$ can form the stable biphase interface with only 1% strain.

It should be emphasized that our results identified the same intermediate, MS2, for the $[3 \times 1]$ and $[1 \times 1]$ intergrowth to form R-MnO_2 and β-MnO_2, respectively. The $[3 \times 1]$ tunnels of MS2 have indeed been identified by TEM.[7,41] The overall barrier to R-MnO_2 and β-MnO_2 differs only by 0.03 eV/fu (0.30 vs 0.33 eV/fu). It is clear that the two transition reactions are highly competing kinetically. The interconversion between R-MnO_2 and β-MnO_2 should also be kinetically feasible since the DFT (HSE06)-predicted energy difference between R-MnO_2 and β-MnO_2 is only 0.05 eV/fu. This explains the in situ XRD data from Shen's work.[15] They found that R-MnO_2 and β-MnO_2 appear sequentially under the same hydrothermal synthetic conditions, and R-MnO_2 is the precursor of β-MnO_2 in their experiment. It is expected that under the synthetic condition (HNO_3 solution, hydrothermal condition), R-MnO_2 becomes thermodynamically less stable than β-MnO_2 and is the kinetically favored product. On the other hand, no transition to α-MnO_2 is found according to XRD data under the same conditions.[15] We attribute this difference between δ to α and δ to β/R transition to the initial nucleation conditions, which select whether the shearing direction is along the $[\bar{2}021]$ direction toward α-MnO_2 or along the $[0\bar{1}11]$ direction toward β/R-phases. Apparently, only the shearing direction along the $[\bar{2}021]$ (or even higher-index) direction can lead to the $[2 \times 2]$ and large tunnels, which in principle have lower kinetic barriers. However, such movements require the collective motion with a larger periodicity, which is not favored for entropic reasons (such collective phonon frequencies are rare in the overall space of vibrational frequency).

3.4. Role of Intercalated K^+ and Self-Doping Mn^{3+} to Phase Transition. One common feature in the phase transition is the breaking the Mn−O bond and the formation of less coordinated Mn (Mn_{4c} or Mn_{5c}) at the TS. From the electronic structure, we found that these low-coordination Mn ions have higher spins up to 3.7, indicating that these Mn are reduced to Mn^{3+} during the reaction. On the other hand, the experimentally synthesized δ-MnO_2 is generally not pure MnO_2 but contains other cations, such as K^+. As a result, the Mn atoms in δ-MnO_2 in the experiment are not formally in the +4 oxidation state but are +3.66 ($K_{0.33}MnO_2$) or even lower (K_xMnO_2, $0.45 < x < 0.67$).[42] From the phase transition mechanism shown above, we expect that these intercalated cations and thus the self-doping Mn^{3+} may play important roles in the phase transition kinetics.

Taking the δ to α transition of $K_{0.125}MnO_2$ as an example (one K atom is intercalated into the interlayer spacing per eight MnO_2 units, as shown in Figure 5), we studied the electronic structure of $K_{0.125}MnO_2$ and searched the reaction pathway for the phase transition. The total DOS of $K_{0.125}MnO_2$ are plotted

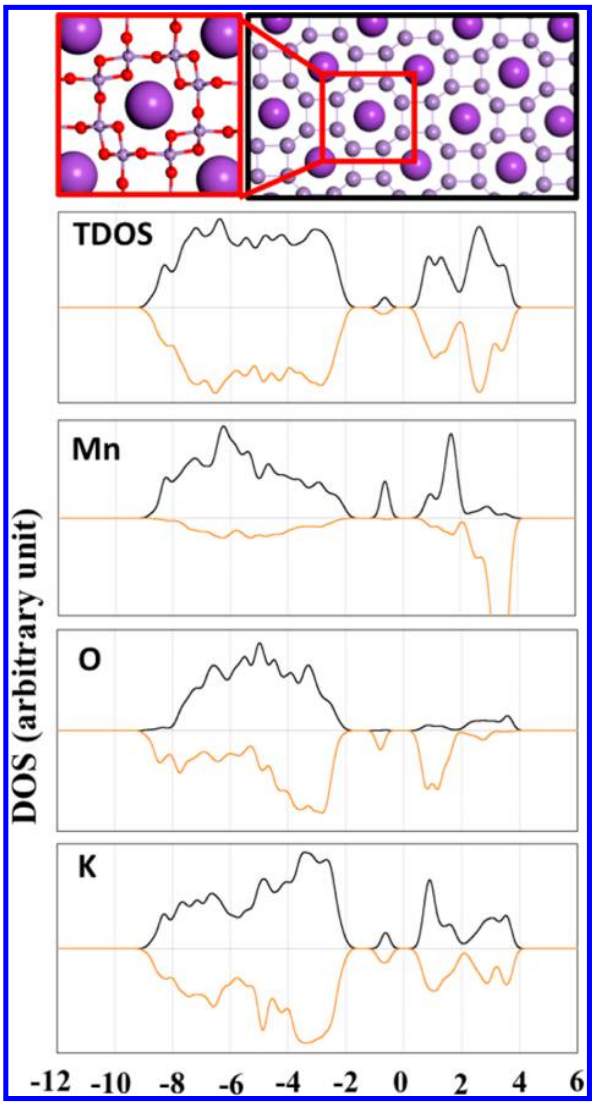

Figure 5. Geometrical structure, spin-resolved total density of states (TDOS), and projected DOS on atoms (Mn, O, K) for α-$K_{0.125}MnO_2$. The large purple balls are the intercalated K^+ (also see Figure 4 caption for the atom style of MnO_2). In the DOS plots, black/red lines represent the majority/minority spin.

in Figure 5 with its projected DOS (PDOS) on K, Mn, and O atoms, which can be compared with those of pure MnO_2 in Figure 2. Interestingly, we found the intercalated K^+ introduces several occupied states within the band gap. These states are delocalized, having significant distributions on all atoms (K, Mn, and O atoms). It implies that the K-intercalated MnO_2 can improve the conductivity of the mateiral. Experimentally, Luo et al. found that the conductivities of K_xMnO_2 increases by following the order of $K_{0.17}MnO_2 > K_{0.15}MnO_2 > K_{0.12}MnO_2 > K_{0.10}MnO_2$ at 273 K.[43]

The reaction pathway for the δ to α transition of $K_{0.125}MnO_2$ has been located using the DESW method by following the same atom displacement pattern shown in Figure 4, and the energy profile is shown in Figure 3b, which compares that of pure MnO_2. We also show the detailed atom movement of the pathway in Figure S1, which highlights the enlarged interlayer spacing (Mn−Mn distance ~6.6 Å) due to the presence of K^+.

DOI: 10.1021/jacs.6b01768
J. Am. Chem. Soc. 2016, 138, 5371−5379

Interestingly, with the intercalating K^+, the transition barrier decreases significantly from 0.17 eV/fu (without K^+) to 0.07 eV/fu, and ΔE also becomes more exothermic by 0.03 eV (Figure 3b). Thus, the intercalated K^+ is predicted to speed up the δ- to α-phase transition that affects mainly the kinetics. In addition to the favorable kinetics toward the $[2 \times 2]$ tunnel, we found that the presence of K^+ ions blocks the transition pathway to form small $[n \times 1]$ tunnel structures such as β- and R-MnO_2 (no transition state can be found for such transition events). Obviously, this is due to the large ionic size of K^+ (effective ionic radii = 1.52 Å[44]) that inhibits the formation of small tunnel structures. This can be clearly seen from thermodynamics. We found that the R-MnO_2 structure with K^+ becomes very unstable, 0.39 eV/fu higher than that of δ-MnO_2 with K^+ according to our DFT calculations. Overall, addition of a K^+ ion is an effective templating strategy to selectively synthesize α-MnO_2, as indeed observed in experiment.[45]

The origin of a lower δ to α transition barrier in $K_{0.125}MnO_2$ can be understood as follows: (i) In K_xMnO_2, the MnO_6 octahedron with Mn^{3+} ($t_{2g}^3e_g^1$) has a strong Jahn−Teller effect, which increases the lengths of two axial Mn^{3+}−O bonds to 2.2 Å and induces the buckling of the MnO_2 sheet. (ii) The barrier height of the phase transition is related to the Mn−O bond strength. In K_xMnO_2, the Mn^{3+}−O bonds are present initially, where one extra electron fills into the antibonding e_g state. The Mn^{3+}−O bond is therefore weaker than Mn^{4+}−O, and it helps to lower the reaction barrier. (iii) The electrostatic interaction between K^+ and the MnO_2 framework can better stabilize the tunnel structures compared to the layer structure. This geometrical effect helps to increase the exothermicity of the reaction.

4. DISCUSSION

According to the topological relation, it is expected that the tunnel structures of MnO_2 should not be limited to $[1 \times 1]$, $[2 \times 1]$, and $[2 \times 2]$ presented above but should also include many other possibilities, such as $[2 \times 3]$, $[2 \times 4]$, and $[3 \times 3]$. Indeed, these frameworks can all exist as stable polymorphs once synthesized[14] and share the common structural features as α- and β-MnO_2, namely, consisting of corner-/edge-sharing MnO_6 octahedra. Apart from the structure change from layer to tunnel at the atomic level, recent experiments[14] have shown that the macroscopic morphology of MnO_2 also varies after the phase transitions from the typical lamellar structure of δ-MnO_2 to the rod/needle shape of the tunnel phases. In addition to this, the macroscopic size of tunnel structures decreases after phase transitions. Naturally, one may wonder what is the general transition pattern to yield tunnel structures, which can drive both the microscopic and the macroscopic change of the phase transition.

From the lowest-energy pathways, we show that while the buckling and shearing of δ-MnO_2 basal plane initiates the phase transition, the tunnel size of the product is, in fact, controlled by the number of MnO_6 octahedra involved in the reaction center, where the Mn−O bonds of MnO_6 octahedra break. For δ to α transition, four MnO_6 octahedra are present as the reaction center, each associated with one Mn−O bond breaking and forming during the reaction (see TS1, Figure 4). By contrast, in the δ to β transition to form the $[1 \times 1]$ tunnels, there are only three MnO_6 octahedra involved for each reaction center (equivalent to a minimal unit cell of 4 MnO_2 fu to describe the phase transition) and, in total, two Mn−O bonds breaking and forming during the reaction (see TS3, Figure 4). We can conclude that the formation of the $[n \times 1]$ tunnel as it appears in the δ to β/R transition requires the minimal number of MnO_6 octahedra (3 MnO_6 octahedra) per reaction center, and the formation of larger tunnels will gradually increase the number of MnO_6 octahedra involved in the reaction center.

To generalize the above finding, we can describe the phase transition pathways of larger pore sizes as follows. For instance, to form the todorokite structure, featuring $[3 \times 3]$ tunnels,[1] we predict that the reaction center needs to involve five edge-sharing MnO_6 octahedra in a row, in which a total of two Mn−O bonds breaks, located at the two ends of the five MnO_6 octahedra row. The mechanism is schematically shown in Figure 6a. In the transition, the MnO_2 sheets buckle and break

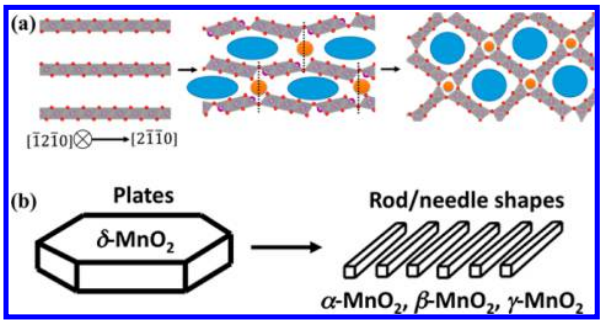

Figure 6. (a) Schematic illustration of the general mechanism for the layer-to-tunnel solid transition by taking todorokite ($[3 \times 3]$) as the example. (b) Schematic diagram for the macroscopic morphology change after phase transitions.

the Mn−O bonds to form individual segments, and each contains a number of edge-sharing MnO_6 octahedra. The number of the MnO_6 octahedra per segment will eventually determine the largest pore size of the material. The Mn−O bonds will rejoin by closing the interlayer spacing at two ends of the segments (indicated by the orange ball in Figure 6a). Finally, the tunnel structures form, with each wall of the tunnel being one of the segments of MnO_2 sheet (indicated by the blue ball). The orange ball regions become the $[1 \times 1]$ tunnel, while the blue ball regions become large tunnels such as $[2 \times 2]$ and $[3 \times 3]$.

According to this general mechanism, the intercalated cations (hydrated cations) should be able to fit into either the orange or the blue ball regions and thus can act as the template to control the pore size of the material. With the increase of the radius of cations, the length of MnO_2 segments needs to increase consistently to encapsulate the cations. Indeed, previous experiments have demonstrated that the presence of K^+ will lead to the formation of $[2 \times 2]$ tunnels, while the smaller radius cations, such as solvated proton, prefer the $[1 \times 1]$ and $[2 \times 1]$ products, and the larger radius ions, such as Mg^{2+}, Co^{2+}, Ni^{2+}, Cu^{2+}, and Zn^{2+}, could lead to even larger pore size.[9]

Knowing the atomic level mechanism, we finally arrive to the position to understand why the macroscopic morphology will change after the solid-phase transition. First, by comparing the mechanical properties of the MnO_2, we found that the δ-MnO_2 has bulk (B) and shear (G) modulus significantly lower than that of other tunnel structures (see Supporting Information Table S2) due to the weak interlayer interaction. The δ-MnO_2 can endure large mechanic distortion, while the other tunnel

DOI: 10.1021/jacs.6b01768
J. Am. Chem. Soc. 2016, 138, 5371−5379

structures do not. Second, the layer-to-tunnel phase transitions are mediated by the intermediate phases, such as MS1 and MS2, which will develop different biphase interfaces. For example, to form the MS1 (the unit cell is defined in Table S1) in the δ to α transition, the $(0001)_{\delta}//(001)_{MS1}$ interface is required. The presence of interfacial strain will help the breaking of the interface along the $[0001]_{\delta}$ direction. As a result, the rod/needle morphology forms after the phase transition. This is schematically shown for the formation of [3 × 3] tunnel in Figure 6a, where the cracking can similarly develop along the $[0001]_{\delta}$ direction, as indicated by the dotted line in the figure.

5. CONCLUSIONS

This work resolves the atomic-level mechanism of the solid-to-solid phase transition in MnO_2, specifically, from the layer phase to the tunnel phases. This reaction is commonly present in many metal oxide systems (e.g., TiO_2, NiOOH) and represents a large family of solid-phase transitions from 2-D material to the interlinked 3-D material. Due to the rich crystal phases of MnO_2, ranging from the layer δ-MnO_2 to differently tunneled α-, β-, and R-phases, the knowledge learned from its solid-phase transition network is of general implications toward a better understanding of other metal oxide transformations that occur under different experimental conditions. The major conclusions achieved in this work are outlined as follows.

(i) All MnO_2 crystal phases studied have similar thermodynamic stabilities at the hybrid HSE06 level, which explains the rich polymorphs of MnO_2 particles. The tunnel structures have VB and CB wider than those of δ-MnO_2 and thus have better electric conductivity.

(ii) The energetic barriers in the lowest-energy pathways for the layer-to-tunnel transitions are generally low, being 0.2−0.3 eV per formula unit. The formations of $[n \times 1]$ tunnels (β- and R-MnO_2) have a slightly higher overall barrier compared to that of $[2 \times 2]$ tunnels (α-phase). The formation of larger tunnels is not favored for entropic reasons.

(iii) All phase transitions initiate via the buckling and shearing movement of δ-MnO_2 basal planes but along different crystallographic directions. The formation of a $[1 \times n]$ tunnel is along the $[0\bar{1}11]$ direction, while that of $[2 \times 2]$ is along the $[\bar{2}021]$ direction. Mn^{3+} is present as the key species in the active center for layer-to-tunnel phase transitions.

(iv) The presence of K cations in MnO_2 can facilitate the layer-to-tunnel, specifically, δ- to α-phase transition, due to the introduction of Mn^{3+}. The selectivity toward different-sized tunnel materials can be tuned by introducing cations.

■ ASSOCIATED CONTENT

Supporting Information

The Supporting Information is available free of charge on the ACS Publications website at DOI: 10.1021/jacs.6b01768.

Lattice constant using DFT+U calculations; bulk and shear modulus for δ-, α-, β-, and R-MnO_2; atomic displacement pattern of δ to α transition for $K_{0.125}MnO_2$; and structures of all IS/TS/FS during phase transition (PDF)

Animation of atomic movement during phase transitions of MS1-K (MOV)

Animation of atomic movement during phase transitions of α (MOV)

Animation of atomic movement during phase transitions of β (MOV)

Animation of atomic movement during phase transitions of α-K (MOV)

Animation of atomic movement during phase transitions of MS1 (MOV)

Animation of atomic movement during phase transitions of MS2 (MOV)

Animation of ramsdellite (MOV)

■ AUTHOR INFORMATION

Corresponding Authors

*yefeil@fudan.edu.cn

*zpliu@fudan.edu.cn

Notes

The authors declare no competing financial interest.

■ ACKNOWLEDGMENTS

This work is supported by National Science Foundation of China (21173051, 21361130019, 21533001, 91545107), 973 program (2011CB808500, 2013CB834603), Science and Technology Commission of Shanghai Municipality (08DZ2270500), Program for Professor of Special Appointment (Eastern Scholar) at Shanghai Institute of Higher Learning, Shanghai Pujiang Program (15PJ1400500), and Shanghai "Chen Guang" project (14CG02).

■ REFERENCES

(1) Golden, D. C.; Chen, C. C.; Dixon, J. B. *Science* **1986**, *231*, 717.

(2) Gorlin, Y.; Lassalle-Kaiser, B.; Benck, J. D.; Gul, S.; Webb, S. M.; Yachandra, V. K.; Yano, J.; Jaramillo, T. F. *J. Am. Chem. Soc.* **2013**, *135*, 8525.

(3) Li, Y.-F.; Liu, Z.-P. *WIREs Comp. Mole. Sci.* **2016**, *6*, 47.

(4) Lang, X.; Hirata, A.; Fujita, T.; Chen, M. *Nat. Nanotechnol.* **2011**, *6*, 232.

(5) Du, W.; Xu, X.; Zhang, D.; Lu, Q.; Gao, F. *Sci. China: Chem.* **2015**, *58*, 627.

(6) Armstrong, A. R.; Bruce, P. G. *Nature* **1996**, *381*, 499.

(7) Post, J. E. *Proc. Natl. Acad. Sci. U. S. A.* **1999**, *96*, 3447.

(8) Chabre, Y.; Pannetier, J. *Prog. Solid State Chem.* **1995**, *23*, 1.

(9) Shen, Y.-F.; Suib, S. L.; O'Young, C.-L. *J. Am. Chem. Soc.* **1994**, *116*, 11020.

(10) Wang, X.; Li, Y. *J. Am. Chem. Soc.* **2002**, *124*, 2880.

(11) DeGuzman, R. N.; Shen, Y.-F.; Neth, E. J.; Suib, S. L.; O'Young, C.-L.; Levine, S.; Newsam, J. M. *Chem. Mater.* **1994**, *6*, 815.

(12) Wang, X.; Li, Y. *Chem. - Eur. J.* **2003**, *9*, 300.

(13) Zhou, F.; Zheng, H.; Zhao, X.; Guo, Q.; Ni, X.; Shen, T.; Tang, C. *Nanotechnology* **2005**, *16*, 2072.

(14) Suib, S. L. *Acc. Chem. Res.* **2008**, *41*, 479.

(15) Shen, X.-F.; Ding, Y.-S.; Hanson, J. C.; Aindow, M.; Suib, S. L. *J. Am. Chem. Soc.* **2006**, *128*, 4570.

(16) Shang, C.; Liu, Z. P. *J. Chem. Theory Comput.* **2013**, *9*, 1838.

(17) Shang, C.; Zhang, X. J.; Liu, Z. P. *Phys. Chem. Chem. Phys.* **2014**, *16*, 17845.

(18) Zhang, X. J.; Shang, C.; Liu, Z. P. *J. Chem. Theory Comput.* **2013**, *9*, 3252.

(19) Zhang, X.-J.; Liu, Z.-P. *J. Chem. Theory Comput.* **2015**, *11*, 4885.

(20) Zhang, X.-J.; Shang, C.; Liu, Z.-P. *J. Chem. Theory Comput.* **2013**, *9*, 5745.

(21) Guan, S.-H.; Zhang, X.-J.; Liu, Z.-P. *J. Am. Chem. Soc.* **2015**, *137*, 8010.

(22) Zhu, S.-C.; Xie, S.-H.; Liu, Z.-P. *J. Am. Chem. Soc.* **2015**, *137*, 11532.

(23) Zhu, S.-C.; Xie, S.-H.; Liu, Z.-P. *J. Phys. Chem. Lett.* **2014**, *5*, 3162.

DOI: 10.1021/jacs.6b01768
J. Am. Chem. Soc. 2016, 138, 5371−5379

(24) Sayle, T. X. T.; Catlow, C. R. A.; Maphanga, R. R.; Ngoepe, P. E.; Sayle, D. C. *J. Am. Chem. Soc.* **2005**, *127*, 12828.
(25) Sayle, T. X. T.; Maphanga, R. R.; Ngoepe, P. E.; Sayle, D. C. *J. Am. Chem. Soc.* **2009**, *131*, 6161.
(26) Tompsett, D. A.; Parker, S. C.; Islam, M. S. *J. Am. Chem. Soc.* **2014**, *136*, 1418.
(27) Kresse, G.; Furthmüller, J. *Phys. Rev. B: Condens. Matter Mater. Phys.* **1996**, *54*, 11169.
(28) Blöchl, P. E. *Phys. Rev. B: Condens. Matter Mater. Phys.* **1994**, *50*, 17953.
(29) Perdew, J. P.; Burke, K.; Ernzerhof, M. *Phys. Rev. Lett.* **1996**, *77*, 3865.
(30) Anisimov, V. I.; Zaanen, J.; Andersen, O. K. *Phys. Rev. B: Condens. Matter Mater. Phys.* **1991**, *44*, 943.
(31) Heyd, J.; Scuseria, G. E.; Ernzerhof, M. *J. Chem. Phys.* **2003**, *118*, 8207.
(32) Cococcioni, M.; de Gironcoli, S. *Phys. Rev. B: Condens. Matter Mater. Phys.* **2005**, *71*, 035105.
(33) Shen, X. F.; Ding, Y. S.; Liu, J.; Cai, J.; Laubernds, K.; Zerger, R. P.; Vasiliev, A.; Aindow, M.; Suib, S. L. *Adv. Mater.* **2005**, *17*, 805.
(34) Franchini, C.; Podloucky, R.; Paier, J.; Marsman, M.; Kresse, G. *Phys. Rev. B: Condens. Matter Mater. Phys.* **2007**, *75*, 195128.
(35) Dong, Y.; Li, K.; Jiang, P.; Wang, G.; Miao, H.; Zhang, J.; Zhang, C. *RSC Adv.* **2014**, *4*, 39167.
(36) Li, F.; Li, G.; Chen, H.; Jia, J. Q.; Dong, F.; Hu, Y. B.; Shang, Z. G.; Zhang, Y. X. *J. Power Sources* **2015**, *296*, 86.
(37) Kramers, H. A. *Physica* **1934**, *1*, 182.
(38) Goodenough, J. B. *Phys. Rev.* **1955**, *100*, 564.
(39) Wiley, J. S.; Knight, H. T. *J. Electrochem. Soc.* **1964**, *111*, 656.
(40) Zhao, W.-N.; Zhu, S.-C.; Li, Y.-F.; Liu, Z.-P. *Chem. Sci.* **2015**, *6*, 3483.
(41) Turner, S.; Gorshkov, A.; Buseck, P. *Advanced Mineralogy: Volume 1 Composition, Structure, and Properties of Mineral Matter: Concepts, Results, and Problems*; Springer-Verlag: New York, 2012, *1*, 101.
(42) Chen, R.; Zavalij, P.; Whittingham, M. S. *Chem. Mater.* **1996**, *8*, 1275.
(43) Luo, J.; Zhu, H. T.; Liang, J. K.; Rao, G. H.; Li, J. B.; Du, Z. M. *J. Phys. Chem. C* **2010**, *114*, 8782.
(44) Shannon, R. D. *Acta Crystallogr., Sect. A: Cryst. Phys., Diffr., Theor. Gen. Crystallogr.* **1976**, *A32*, 7510.
(45) Yuan, Y.; Wood, S. M.; He, K.; Yao, W.; Tompsett, D.; Lu, J.; Nie, A.; Islam, M. S.; Shahbazian-Yassar, R. *ACS Nano* **2016**, *10*, 539.

DOI: 10.1021/jacs.6b01768
J. Am. Chem. Soc. 2016, 138, 5371−5379